## PAPER

# Unveiling the relationship between counterion size and spin crossover dynamics in hexadentate Schiff-base manganese(III) complexes†

Meng-Jia Shang,[a] Du-Yong Chen,[a] Ren-He Zhou,[a] Han-Han Lu,[a] Lin Ma,[a] Jingyi Xiao,[b] Liang Zhao,[a] Yin-Shan Meng ⓘ *[a,c] and Tao Liu ⓘ *[a,c]

Understanding the relationship between molecular packing/interaction and the spin crossover property is essential for advancing solid-state molecular memory devices. In this work, a series of hexadentate Schiff-base manganese(III) complexes ([Mn(4F-sal$_2$323)]X, X = ClO$_4$ (**1**); X = AsF$_6$ (**2**); X = PF$_6$ (**3**); X = ReO$_4$ (**4**) and X = NO$_3$ (**5**)) were synthesized and characterized. Magnetic studies showed that complex **1** exhibited an abrupt spin transition at 90 K with a 10 K wide thermal hysteresis, while complexes **2–5** exhibited gradual and incomplete spin transition with no hysteresis. Analysis of the magneto-structural correlation indicated that the SCO transition temperature is negatively correlated with the octahedral distortion and void space volume of the anions. Detailed variable-temperature structural analysis revealed that hydrogen bonding interaction and close stacking hinder the torsional deformation of the Mn$^{III}$ coordination sphere, preventing complete SCO. Density functional theory (DFT) calculations revealed that the weaker hydrogen bonding in complex **1** led to lower atomic charges on the nitrogen atoms, thereby affecting the coordination field strength of the Mn center. This work demonstrates that the transition temperature of SCO is influenced by supramolecular stacking forces, and this relationship can be finely tuned by simply adjusting the size of the ions.

## Introduction

Spin crossover (SCO) is a phenomenon observed in first-row transition metal complexes with a 3d$^n$ ($n$ = 4–7) electronic configuration, where the complexes undergo a reversible transformation between the low-spin (LS) and high-spin (HS) states.[1–4] This spin state transition can be induced by external stimuli, such as temperature, light, pressure, magnetic fields, pH and guest molecules.[5–9] One of the most common manifestations is temperature-dependent spin state switching.[10–13] This stimuli-responsive nature endows bistable SCO complexes with potential applications in advanced technologies,

especially in memory devices designed for high-density information storage and processing.[14,15] A broad hysteresis loop is essential for enhancing memory effects, and considerable research efforts have been directed toward developing SCO systems with wide hysteresis loops that function near room temperature.[16,17]

Among the reported hysteretic spin crossover (SCO) systems, Fe$^{II}$-based (3d$^6$) complexes are particularly well-known, especially those with polymeric structures featuring triazole ligands or Hofmann-type frameworks with pyrazine ligands.[18,19] Although a few hysteretic SCO complexes have been identified for Fe$^{III}$- (3d$^5$) and Co$^{II}$-based (3d$^7$) ones,[20–22] reports on Mn$^{III}$-based (3d$^4$) complexes remain relatively rare. The first Mn$^{III}$ SCO complex, [Mn(pyrol)$_3$tren], was identified by Sinn and Sim in 1981.[23] This mononuclear chelate Mn$^{III}$ complex exhibits an abrupt, temperature-dependent SCO behavior. Thirty years later, Morgan *et al.* reported the first Mn$^{III}$-based complex featuring a cooperative spin transition, [Mn(sal-N-1,5,8,12)]PF$_6$, which displayed an 8 K wide hysteresis loop.[24] Notably, [Mn(5-Cl-sal-N-1,5,8,12)]TCNQ$_{1.5}$·2CH$_3$CN showed an exceptionally wide hysteresis loop of 50 K, which remains a record for this class of complexes.[25] According to the ligand field theory, spin crossover (SCO) is theoretically feasible for octahedral 3d$^4$–3d$^7$ metal ions.[26] However, SCO phenomena

*[a]State Key Laboratory of Fine Chemicals, Frontier Science Center for Smart Materials, School of Chemical Engineering, Dalian University of Technology, No. 2 Linggong Road, Dalian 116024, China*

*[b]Instrumental Analysis Center, Dalian University of Technology, No. 2 Linggong Road, Dalian 116024, China*

*[c]Liaoning Binhai Laboratory, Dalian 116023, China. E-mail: mengys@dlut.edu.cn, liutao@dlut.edu.cn*

are particularly rare in 3d$^4$ metal complexes, where the high-spin state is typically stabilized by the Jahn–Teller effect.[27] Consequently, organic ligands capable of generating an appropriate ligand field strength on the Mn$^{III}$ center to induce SCO are limited, making the rational design, synthesis, and investigation of Mn$^{III}$ SCO complexes with wide hysteresis loops a challenging task. One promising candidate is the ligand sal$_2$-323 (2,2′-((1$E$,13$E$)-2,6,9,13-tetraazatetradeca-1,13-diene-1,14diyl) diphenol), which employs the flexible $N$,$N$′-bis (3-aminopropyl) ethylenediamine as a linker.[28,29] This modification extends the bridge by two methylene groups, resulting in a *trans*-arrangement of the phenolate donor oxygens. This structural arrangement induces notable Jahn–Teller distortions, characterized by axial compression of Mn–O bonds and equatorial elongation of Mn–N bonds, which in turn facilitate the SCO.[30,31] However, most Mn$^{III}$ SCO complexes with sal$_2$-323 and its derivatives exhibit gradual and incomplete SCO behavior.[32–34]

Given the small energy difference between the LS and HS states in Mn$^{III}$ complexes, designing new Mn(III) SCO complexes with strong cooperative effects, such as abrupt SCO curves, high transition temperatures, and wide hysteresis loops, is challenging.[35,36] On the other hand, predicting and rationalizing structural motifs for tuning SCO properties and transition temperatures in the solid state is difficult due to the influence of substituents, counterions, and co-crystallized solvent molecules.[37–41] In addition, intermolecular interactions like hydrogen bonding and π···π stacking, as well as structural phase transitions also affect the formation of highly cooperative systems with abrupt and hysteretic spin transitions.[42–45] Magneto-structural correlations can only be established in rare cases where SCO complexes are isomorphous (share the same space group, unit cell dimensions and similar types/positions of atoms) or isostructural (differ in space group and unit cell parameters, but retain similar types/positions of atoms and molecular arrangements in the crystal).[46] Thus, in the solid state, few reliable relationships between transition temperature and ligand or anion choices can be made.[47]

In this work, we aimed to verify how counterions and intermolecular interactions influence the SCO property. We synthesized a 4-fluoro-substituted hexadentate Schiff-base, namely 4F-sal$_2$323 (6,6′-((1$E$,13$E$)-2,6,9,13-tetraazatetradeca-1,13-diyl)bis(3-fluorophenol)), to provide an appropriate ligand field for SCO of the Mn$^{III}$ center, and accordingly introduced various anions with different sizes and configurations. A family of new complexes ([Mn(4F-sal$_2$323)X], X = ClO$_4$ (**1**); X = AsF$_6$ (**2**); X = PF$_6$ (**3**); X = ReO$_4$ (**4**) and X = NO$_3$ (**5**)) was synthesized. Complex **1** exhibited an abrupt spin crossover with a 10 K thermal hysteresis, while complexes **2–5** exhibited gradual and incomplete spin transition curves without hysteresis. Notably, as the effective 'void' space volume increased, the transition temperature of the Mn$^{III}$ SCO complexes decreased. In this system, all complexes were crystallized without any lattice solvents and exhibited the same configuration, thus providing an ideal platform to study the effects of ion pairs on the cooperativity in Mn$^{III}$ SCO systems. Herein, we show the detailed characterization and discussion results.

# Experimental section

## Materials and synthesis

All chemical reagents were acquired from commercial sources and used without further purification. The ligands were synthesized according to the methods in the literature.[48]

**Synthesis of [Mn(L)]ClO$_4$ (1).** To a solution of $N$,$N$′-bis(3-aminopropyl)ethylenediamine (0.174 g, 1 mmol) in methanol (10 mL) was added 4-fluoro-2-hydroxybenzaldehyde (0.28 g, 2.0 mmol) in methanol (10 mL). The solution was stirred at room temperature for a further 30 min, after which time a solution of manganese(II) perchlorate hexahydrate (0.251 g, 1 mmol) in methanol (20 mL) was added; the solution changed from yellow to deep brown and was stirred for 10 min, and the product crystallized by slow evaporation of solvent after filtration (0.234 g, 41%). Elemental analysis (%) calculated for C$_{22}$H$_{26}$ClF$_2$MnN$_4$O$_6$: C, 46.29; H, 4.59; N, 9.81. Found: C, 46.51; H, 4.74; N, 9.56.

**CAUTION!** Perchlorate is potentially explosive and should be used in small quantities and with utmost care at all times.

**Synthesis of [Mn(L)]AsF$_6$ (2).** The synthesis method is the same as for complex **1**, except that manganese perchlorate is replaced by manganese(II) chloride tetrahydrate (0.197 g, 1 mmol) and sodium hexafluoroarsenate (423.8 g, 2.0 mmol). Black crystals formed upon evaporation of solvent within a week (0.211 g, 32%). Elemental analysis (%) calculated for C$_{22}$H$_{26}$AsF$_8$MnN$_4$O$_2$: C, 40.02; H, 3.97; N, 8.80. Found: C, 40.34; H, 3.87; N, 8.49.

**Synthesis of [Mn(L)]PF$_6$ (3).** The synthesis method is the same as for complex **1**, except that manganese perchlorate is replaced by manganese(II) chloride tetrahydrate (0.197 g, 1 mmol) and ammonium hexafluorophosphate (326 g, 2.0 mmol). Black crystals formed upon evaporation of solvent within a week (0.136 g, 22%). Elemental analysis (%) calculated for C$_{22}$H$_{26}$F$_8$MnN$_4$O$_2$P: C, 42.87; H, 4.25; N, 9.09. Found: C, 42.61; H, 4.18; N, 9.31.

**Synthesis of [Mn(L)]ReO$_4$ (4).** The synthesis method is the same as for complex **1**, except that manganese perchlorate is replaced by manganese(II) chloride tetrahydrate (0.197 g, 1 mmol) and sodium perrhenate (0.546 g, 2.0 mmol). Black crystals formed upon evaporation of solvent within a week (0.181 g, 25%). Elemental analysis (%) calculated for C$_{22}$H$_{26}$F$_2$MnN$_4$O$_6$Re: C, 36.62; H, 3.63; N, 7.76. Found: C, 36.42; H, 3.58; N, 7.98.

**Synthesis of [Mn(L)]NO$_3$ (5).** The synthesis method is the same as for complex **1**, except that manganese perchlorate is replaced by manganese(II) nitrate tetrahydrate (0.251 g, 1 mmol), and the product crystallized by slow evaporation of solvent after filtration (0.128 g, 24%). Elemental analysis (%) calculated for C$_{22}$H$_{26}$F$_2$MnN$_5$O$_5$: C, 49.54; H, 4.90; N, 13.62. Found: C, 49.71; H, 4.84; N, 13.41.

## Physical measurements

**X-ray data collection and structure determinations.** The single-crystal X-ray diffraction data were collected using a Bruker D8 Venture CMOS–based diffractometer (Mo-Kα radiation, $\lambda$ = 0.71073 Å). The structures were solved with the ShelXT program using the intrinsic phasing method and refined with the ShelXL refinement package using least squares minimization. All non-hydrogen atoms were subjected to anisotropy treatment, while hydrogen atoms were determined by electron cloud density maps or theoretical hydrogenation. The powder X-ray diffraction (PXRD) data were obtained using a Bruker AXS D8 Advance X-ray powder diffractometer with Cu-Kα radiation ($\lambda$ = 1.5418 Å) to verify the purity of the crystals.

**Thermogravimetric analysis (TGA) and elemental analysis.** Thermogravimetric analysis was performed under a nitrogen atmosphere at a heating rate of 10 °C min$^{-1}$ using the TG/DTA Q600 system. Elemental analyses for C, H, and N were performed using an Elementar Vario EL Cube elemental analyzer.

**Magnetic measurements.** The magnetic properties were characterized using a Quantum Design Dynacool PPMS-9 instrument. During measurement, all samples were in the form of microcrystalline powder, wrapped in a sealing film, and filled into diamagnetic capsules. The temperature change rate during magnetic testing was 2 K min$^{-1}$. During data processing, the Pascal constant is used to perform background demagnetization correction on the sealing film and capsule used.

**UV-vis absorption spectroscopy.** UV-vis-NIR absorption spectroscopy was performed using a HITACHI UV-vis spectrophotometer (UH4150). The UV-vis spectroscopic measurements in solution were performed in quartz cuvettes with a path length of 1 cm.

**Dielectric permittivity measurements.** Temperature-dependent alternating current (AC) dielectric permittivity measurements were conducted using the Quantum Design PPMS-9 system with a KEYSIGHT E4980AL meter, applying a voltage of 2.0 V. The temperature sweep was performed at a rate of 1 K min$^{-1}$ within the range of 70–340 K. For dielectric measurements, samples were prepared with electrodes attached using silver conducting glue.

**Electrochemistry measurements.** Electrochemistry experiments were performed using a Metrohm Autolab PGSTAT101 system using platinum as the working electrode in acetonitrile with 0.2 M ($^n$Bu$_4$)NPF$_6$ as supporting electrolyte. Ag/AgCl was used as an internal reference.

# Results and discussion

The condensation reaction of 4-fluoro-2-hydroxybenzaldehyde with 1,2-bis(3-aminopropylamino)ethane in a 2 : 1 molar ratio afforded a hexadentate Schiff-base ligand (Scheme 1). Subsequent coordination with Mn$^{2+}$ salts resulted in aerial oxidation, leading to the formation and crystallization of a series of mononuclear Mn$^{3+}$ complexes as dark red to black crystals. The perchlorate and nitrate derivatives were synthesized directly from the corresponding manganese(II) salts, whereas the remaining complexes were obtained *via* salt metathesis reactions. Powder X-ray diffraction experiments were performed to confirm the phase purities of the bulk polycrystalline materials (Fig. S1†). These crystals were structurally characterized by single-crystal X-ray diffraction at 300 K. Selected crystallographic data and structure refinements are summarized in Tables S1–S5.† Compounds **1–5** crystallize in the non-centrosymmetric orthorhombic space group $P2_12_12_1$, except for complex **4**, which crystallizes in the monoclinic space group $P2_1/n$. The asymmetric unit of complexes **1–5** consists of a mono-cationic [Mn(4F-sal$_2$-323)]$^+$ component and a counter anion (ClO$_4^-$, AsF$_6^-$, SbF$_6^-$, ReO$_4^-$, NO$_3^-$, respectively) (Fig. 1). For all complexes, no solvent molecules are found in the crystal lattice, which is consistent with the results of the TGA analysis (Fig. S2†). Complexes **1–5** possess a similar distorted octahedral geometry with an MnN$_4$O$_2$ configuration (evaluated by Continuous Shape Measures (CShM), Tables 1 and S12†), where the equatorial and axial positions are occupied by four nitrogen donor atoms (two amines and two imines) in *cis*-amine and *cis*-imine configurations and two oxygen donor atoms, respectively, coming from the hexadentate ligand.

Since complexes **1–5** possess very similar structures, we will take complex **1** as the example to describe the structural
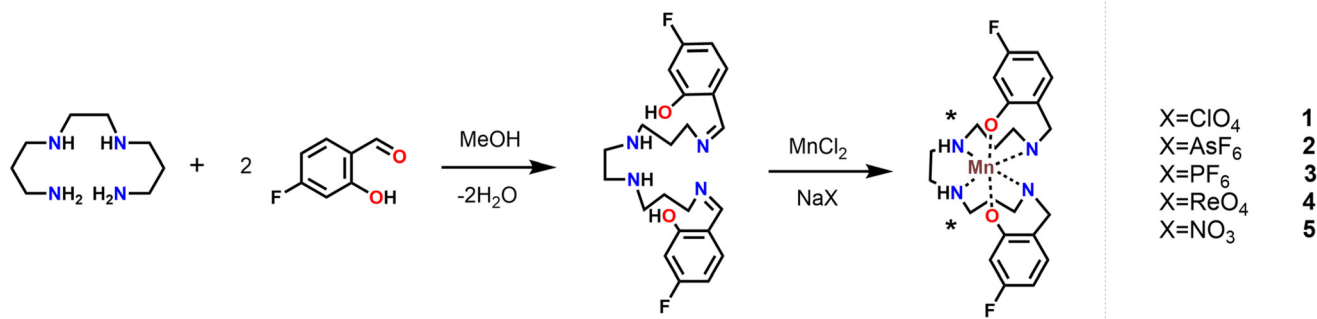
**Scheme 1** . Schematic illustration of the structure of complexes **1–5**.
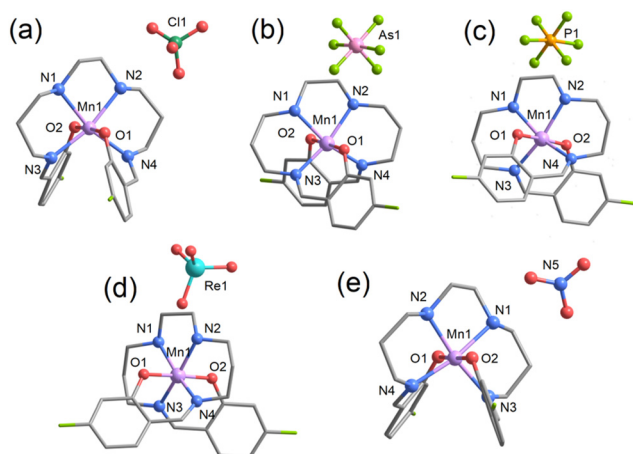
Fig. 1  The crystal structures of complexes **1** (a), **2** (b), **3** (c), **4** (d), and **5** (e) at 300 K. Color code: Mn, bright purple; C, grey; N, blue; O, red; F, pale yellow; Cl, green; As, pink; P, orange; Re, sky blue. Hydrogen atoms are omitted for clarity.
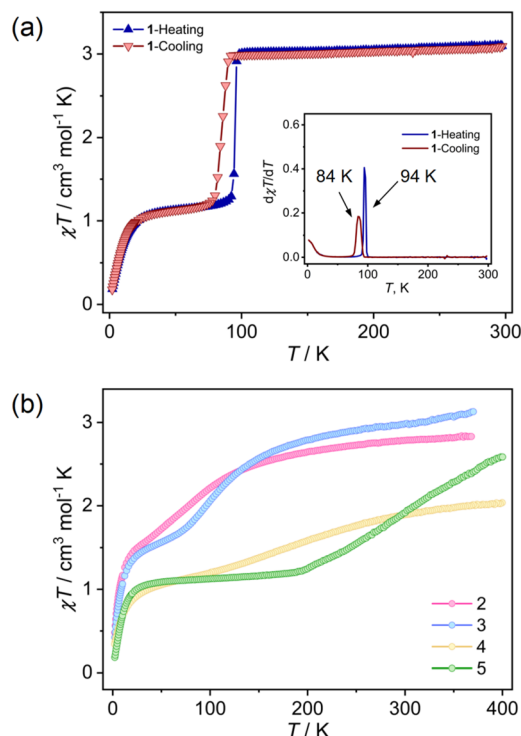


Fig. 2  (a) Magnetic susceptibility curves for complexes **1** in the heating and cooling modes; (b) magnetic susceptibility curves for complexes **2–5**.

details of each. A representation of the molecular structure of **1** at 300 K is depicted in Fig. 1a revealing that the asymmetric unit comprises one discrete mononuclear $[Mn(4F\text{-}sal_2\text{-}323]^+$ cation and one $ClO_4^-$ anion. The pseudo-octahedral geometry is formed by *trans*-O donors and pairs of *cis*-imine and *cis*-amine nitrogen atoms in the equatorial plane. At 300 K, the Mn–N$_{amine}$ (N1 and N2), Mn–N$_{imine}$ (N3 and N4) and axial Mn–O (O1 and O2) distances are 2.186(4)–2.219(4), 2.090(4)–2.103(4) and 1.879(3)–1.881(3) Å, respectively, showing an average Mn–N/O bond distance of 2.060 Å (Table S11†). These values lie within the bond distances observed for a HS Mn$^{III}$ center in an MnN$_4$O$_2$ coordination sphere.[49] When decreasing the temperature to 60 K, Mn–N$_{amine}$ and Mn–N$_{imine}$ bond lengths show a sizeable decrease to 2.050(9)–2.060(2) Å, and 1.988(2)–1.997(2) Å, respectively, with an average Mn–N/O bond distance of 1.977 Å. These values are in the range expected for LS Mn$^{III}$. The overall structural studies described the spin-state switching from the HS state at 300 K to the LS state at 60 K, which is consistent with the magnetic studies (Fig. 2a). It is noted that the difference between the average Mn–N/O distances in the

HS (300 K) and LS states (60 K) for complex **1** is 0.083 Å, which lies in the range expected for manganese(III) SCO systems, where a single electron transfer occurs between antibonding ($t^3_{2g}e^1_g$; HS) and bonding ($t^4_{2g}e^0_g$; LS) orbitals upon spin-state switching. In addition, during spin-state switching from the HS state to the LS state a significant decrease in the Mn–N$_{amine}$ and Mn–N$_{imine}$ bond distances was observed while the Mn–O bonds remained nearly unchanged, which can be described by the depopulation of the antibonding $d_{x^2-y^2}$ orbital. It is interesting that when heating the crystal from 60 to 85 K, the Mn–N$_{amine}$, Mn–N$_{imine}$ and axial Mn–O distances are nearly unchanged, showing distances of 2.036(1)–2.080(9),

Table 1  The structural distortion parameters of the Mn site for complexes **1–5**

| Complex | **1**-ClO$_4$ | | **2**-AsF$_6$ | | **3**-PF$_6$ | | **4**-ReO$_4$ | | | **5**-NO$_3$ | | |
|---|---|---|---|---|---|---|---|---|---|---|---|---|
| $T$ (K) | 60 | 300 | 35 | 300 | 35 | 300 | 60 | 300 | 400 | 120 | 300 | 400 |
| $\Sigma_{Mn}{}^a$ (°) | 21.88 | 53.12 | 34.20 | 57.26 | 36.46 | 55.72 | 26.027 | 44.237 | 48.55 | 30.35 | 40.847 | 49.57 |
| $\Theta^b$ (°) | 48.37 | 100.015 | 59.648 | 100.105 | 69.254 | 99.371 | 53.668 | 79.735 | 85.191 | 51.830 | 66.43 | 79.025 |
| $\alpha^c$ (°) | 39.845 | 45.557 | 46.647 | 52.456 | 46.464 | 50.637 | 39.455 | 43.077 | 44.349 | 54.792 | 54.920 | 55.667 |
| $\zeta^d$ (Å) | 0.373 | 0.719 | 0.448 | 0.762 | 0.506 | 0.753 | 0.352 | 0.587 | 0.626 | 0.367 | 0.479 | 0.580 |
| CShM$_{Mn}{}^e$ | 0.271 | 1.350 | 0.461 | 1.371 | 0.591 | 1.373 | 0.285 | 0.802 | 0.950 | 0.290 | 0.525 | 0.813 |
| $\Delta\Sigma$ | 31.24 | | 23.06 | | 19.26 | | 22.52 | | | 19.22 | | |
| $\Delta\Theta$ | 51.645 | | 40.457 | | 30.117 | | 31.523 | | | 27.195 | | |

$^a$ The sum of the deviation from 90° of the 12 *cis*-angles of the MnN$_4$O$_2$ octahedron. $^b$ The sum of the deviation from 60° of the 24 trigonal angles of the projection of the MnN$_4$O$_2$ octahedron onto the trigonal faces. $^c$ The dihedral angle between the least-squares planes of the two phenolate rings. $^d$ The sum of deviation from individual M–X bond distances with respect to the mean metal–ligand bond distance. $^e$ The continuous shape measurement relative to the ideal octahedron of the Mn centers; a zero value corresponds to the ideal octahedron geometry.

1.982(9)–1.992(9) and 1.881(9)–1.883(8) Å, respectively. These values indicate that Mn$^{III}$ retains its LS state. Conversely, when cooling the crystal from 300 to 85 K, the Mn–N$_{amine}$, Mn–N$_{imine}$ and axial Mn–O distances are 2.190(9)–2.237(9), 2.070(8)–2.112(9) and 1.878(7)–1.880(7) Å, indicating that Mn$^{III}$ is in a HS state. The crystal structure analysis indicated that complex **1** underwent a hysteretic SCO.

Magnetic susceptibilities of **1** were recorded in cooling and warming modes under an applied dc field of 1000 Oe and temperature sweeping rate of 2 K min$^{-1}$ in the temperature range 2–300 K, as shown in the $\chi T$ versus $T$ plots in Fig. 2a, where $T$ represents the absolute temperature and $\chi_M$ denotes the molar magnetic susceptibility. At room temperature, the $\chi_M T$ value of 3.09 cm$^3$ K mol$^{-1}$ for **1** is typical for a HS Mn$^{III}$ ion (with $S = 2$, $g = 2$).[50] With decreasing temperature, the $\chi_M T$ value remained constant on cooling to 92 K and then dropped sharply to 1.24 cm$^3$ K mol$^{-1}$ at 78 K with critical temperature $T_{1/2}\downarrow = 84$ K. The $\chi_M T$ value of 1.09 cm$^3$ K mol$^{-1}$ at 20 K indicated full conversion to the LS state ($S = 1$). Below 20 K, the $\chi_M T$ value dropped to 0.36 cm$^3$ K mol$^{-1}$, which is consistent with the zero-field-splitting (ZFS) effect. Upon warming, an abrupt transition was observed but with $T_{1/2}\uparrow = 94$ K, resulting in a thermal magnetic hysteresis loop of 10 K width.

However, complex **2** showed a gradual SCO with $\chi_M T$ falling slowly from 2.93 cm$^3$ K mol$^{-1}$ at 300 K to 1.43 cm$^3$ K mol$^{-1}$ at 20 K (Fig. 2b). This value is consistent with a HS/LS ratio of 22 : 78. Below 20 K, the $\chi_M T$ value decreases sharply due to the zero-field-splitting effect. The $\chi_M T$ value of complex **3** at 300 K is 3.13 cm$^3$ K mol$^{-1}$, which is higher than the expected value of 3.00 cm$^3$ K mol$^{-1}$ for complete HS Mn$^{III}$ ions. During the crystal cooling process, the $\chi_M T$ value decreased slowly until reaching 2.72 cm$^3$ K mol$^{-1}$ at 180 K, with a more rapid decrease below this temperature. With temperature decreasing to 50 K, the $\chi_M T$ value decreased to 1.56 cm$^3$ K mol$^{-1}$. Upon further cooling, complex **3** shows an incomplete conversion to the 84% LS state with the $\chi_M T$ value of 1.34 cm$^3$ K mol$^{-1}$ at 20 K. Below 20 K, due to the ZFS of Mn$^{III}$, the $\chi_M T$ value decreased very quickly to 0.42 cm$^3$ K mol$^{-1}$ at 2 K. At 300 K, the average Mn–N/O bond distances of complexes **2** and **3** are 2.057 and 2.058 Å, respectively, which are within the range expected for HS Mn(III). Upon cooling to 35 K, these values decrease to 1.995 and 2.003 Å, respectively, indicating a partial transition of Mn(III) to low-spin (LS) states. Such bond distance variations are consistent with the magnetic measurement data.

Complexes **4** and **5** demonstrate an incomplete gradual SCO behavior in the testing temperature range. They have similar SCO profiles, although that of complex **4** is slightly more gradual. At 100 K, the $\chi_M T$ values (1.05 cm$^3$ K mol$^{-1}$ for **4** and 1.03 cm$^3$ K mol$^{-1}$ for **5**) are close to the expected LS value of 1.0 cm$^3$ K mol$^{-1}$. Complex **4** undergoes SCO above 50 K, and the $\chi_M T$ value gradually increases until it reaches 2.04 cm$^3$ K mol$^{-1}$ at 370 K. Complex **5** started to switch from LS to HS at approximately 200 K, and then the $\chi_M T$ value rapidly increases, reaching 2.58 cm$^3$ K mol$^{-1}$ at 370 K. The average Mn–N/O bond distances of complexes **4** and **5** are 1.981 (60 K) and

1.971 Å (120 K), respectively. These values are in the range expected for LS Mn$^{III}$. Upon heating to 400 K, Mn–N bond lengths showed an increase to 2.045 Å and 2.023 Å, respectively, showing that partial Mn$^{III}$ ions have transformed into the HS state.

In short, complexes **1–5** exhibit different SCO behaviors. The transition temperatures are in the order **5 > 4 > 1 > 3 > 2**. The spin state of Mn$^{III}$ can be inferred in Table S11.† All SCO complexes show an increase in Mn–N$_{amine}$ and Mn–N$_{imine}$ distances upon warming, but no significant changes occur in the Mn–O$_{phen}$ bond lengths. Therefore, the change in the Mn$^{III}$ coordination sphere during the spin transition event is anisotropic, manifesting as compression or elongation within the equatorial plane. This structural alteration can be attributed to the Jahn–Teller distortion, which is accommodated by the population of the antibonding d$_{x^2-y^2}$ orbital in the MnN$_4$ plane upon transition to the high-spin (HS) state. Additionally, it is found that the overall bond length changes during spin transitions in Mn$^{III}$ complexes **1–5** are smaller compared to those in Fe$^{II}$ or Fe$^{III}$ complexes. Unlike d$^5$ or d$^6$ complexes, where the spin transition involves the switching of two electrons between the t$_{2g}$ and e$_g$ orbitals, in d$^4$ Mn$^{III}$ complexes, only one electron is transferred between the low-spin (t$_{2g}^4$e$_g^0$, $S = 1$) and high-spin (t$_{2g}^3$e$_g^1$, $S = 2$) states.

The spin crossover (SCO) is also manifested through changes in the average trigonal distortion angle ($\Theta$) and the octahedral distortion parameter ($\Sigma$).[51] These parameters serve as indicators of the extent of deviation from the ideal octahedral coordination geometry (where $\Sigma$ and $\Theta$ are 0). Additionally, the distortions in the Mn$^{III}$ coordination geometry can be quantified using parameters $\zeta$ and $\alpha$, where $\alpha$ represents the dihedral angle between the least-squares planes of the two phenolate rings, and $\zeta$ denotes the sum of deviations in individual M–X bond lengths relative to the average metal–ligand bond distance. Structural distortions occurring during spin-state transitions were examined by calculating the octahedral distortion parameters at both low and high temperatures (Table 1). The $\Sigma$, $\Theta$, $\zeta$, and $\alpha$ values for complex **1** at 120 K are 52.93°, 102.813°, 42.879°, and 0.734 Å, respectively. Upon lowering the temperature to 60 K, these values decreased significantly to 21.88°, 48.37°, 39.845°, and 0.373 Å, which suggests that complex **1** is closer to the ideal octahedron in the LS state. For complexes **2–5**, all these parameters of the HS state are higher than those of the LS state. This can be understood from the fact that the population of antibonding orbitals of HS Mn$^{III}$ leads to a more distorted coordinating geometry from a perfect octahedron.

For this series of complexes [Mn(4F-sal$_2$323)]X, a correlation exists between $T_{1/2}$ and $\Sigma_{Mn}$. The $T_{1/2}$ values for the complexes **1–5** are 94, 82, 92,192 and 294 K, respectively (Fig. S3†). As shown in Fig. 3, the $T_{1/2}$ was negatively correlated with the $\Sigma_{Mn}$ parameter for complexes **1–5** at 300 K. A higher $\Sigma_{Mn}$ value is invariably associated with a greater rearrangement of the molecular lattice, which introduces an unfavorable barrier to the SCO process, leading to the observed inverse relationship between $T_{1/2}$ and $\Sigma_{Mn}$. Conversely, smaller $\Sigma_{Mn}$ values are gen-
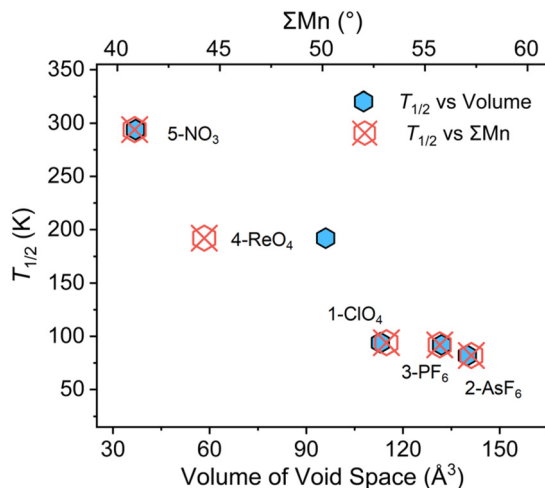
**Fig. 3** Plots of the experimental $T_{1/2}$ value *versus* the $\Sigma_{Mn}$ value or the volume of the 'void' space for complexes **1**–**5** at 300 K.

erally associated with a stronger ligand field, thereby stabilizing the LS state of the $Mn^{III}$ ion.

On the other hand, the size of counterions can influence $\Sigma_{Mn}$, thereby affecting the ligand field around the $Mn^{3+}$ center and regulating $T_{1/2}$. Comparing the $T_{1/2}$ of complexes **1**–**5** with their respective ionic volumes revealed that, except for complex **1**, larger anion volumes generally result in lower $T_{1/2}$ (Fig. S4†). Since the lattice lacks solvent, the theoretical 'void' space volume (occupied by spin-inactive species in the absence of anions) was also considered. The Mercury program was then used to calculate the void space with a probe radius of 1.2 Å and approximate grid spacing of 0.2 Å.[46] The void space percentage in the unit cell and the volume of void space per cation were calculated (Fig. S5 and Table S13†). Noting that the packing motifs of complexes **1**–**5** are identical, a direct comparison can thus be made between this series of complexes and their respective SCO properties, which is not always possible, as many families of SCO complexes pack into different lattices affecting the SCO pathway. A trend was observed: larger "void" volumes correspond to lower $T_{1/2}$ values (Fig. 3). Larger anion volumes produce greater void spaces, allowing the spin-active species, which allows the spin-active species $[Mn(4F\text{-}sal_2323)]^+$ to undergo a larger $\Sigma_{Mn}$, thereby stabilizing the HS state and resulting in a lower $T_{1/2}$. In contrast, smaller anion volumes result in smaller void spaces, restricting molecular lattice rearrangements and favoring the more compact LS state, thereby increasing $T_{1/2}$.

It is considered that the SCO behavior is also related to the intra- and intermolecular interactions induced by different counterions. Complex **1** has a small anion volume but a relatively large inactive cavity volume. Close inspection of the crystal structures revealed the strong hydrogen bonding interactions between the $[Mn(4F\text{-}sal_2323)]^+$ cation and the counterions in complexes **2**–**5**. Interestingly, in complex **1**, only weak interactions are present, and no strong hydrogen bonding interactions like this are observed, despite the latter exhibiting

significant hysteretic SCO behavior. Hirshfeld surface analyses[52] were conducted to critically evaluate the intermolecular interactions in complexes **1**–**5**. A comprehensive description is provided using complex **1** as a representative example. The three-dimensional $d_{norm}$ surface of complex **1** at both 300 K and 60 K, using a standard surface resolution, is shown in Fig. S6 and S7.† The Hirshfeld surface, mapped with electrostatic potential, reveals blue regions indicative of positive electrostatic potential, while bright-red spots correspond to atoms with a negative electrostatic potential. These intense red spots on the surface arise from N–H⋯O, C–H⋯O, and C–H⋯F interactions, all of which have distances greater than 3.1 Å (Fig. 4a). The fingerprint plots for complex **1** at 300 K showed characteristic pseudo-symmetric wings along the $d_e$ and $d_i$ diagonal axes, which are attributed to the H⋯H, H⋯O/O⋯H, H⋯F/F⋯H, C⋯H/H⋯C and C⋯F/F⋯C interactions (Fig. S6†). Specifically, in terms of H⋯H contacts, the intermolecular interactions at 300 K are reflected by the distribution of the scattered points in the fingerprint plots, which extend to $d_e = d_i = 1.0$ Å in complex **1**, contributing 37.1% of the total Hirshfeld surface area (Fig. S6b†), the highest among all interactions. In addition, the O⋯H/H⋯O interactions contribute 20.4% of the total Hirshfeld surface area (Fig. S6c†). Among these, the H⋯O (19.1%) interactions corresponding to N–H⋯O interactions make a larger contribution than the O⋯H (1.3%) interactions, which are represented by the spikes in the bottom right and left regions ($d_e + d_i \approx 1.75$ Å). The relative contributions to the Hirshfeld surface of all the contacts in complex **1** at 300 K and 60 K are summarized. Compared to complex **1** at 300 K, the contribution from O⋯H/H⋯O contacts to the Hirshfeld surface increases at 60 K. In addition, hydrogen bond distances (Å) and angles (°) for **1**-ClO$_4$ at 60 K and 300 K are listed in Table S14.† In summary, the Hirshfeld surface analysis proves that complex **1** exhibits weak inter-
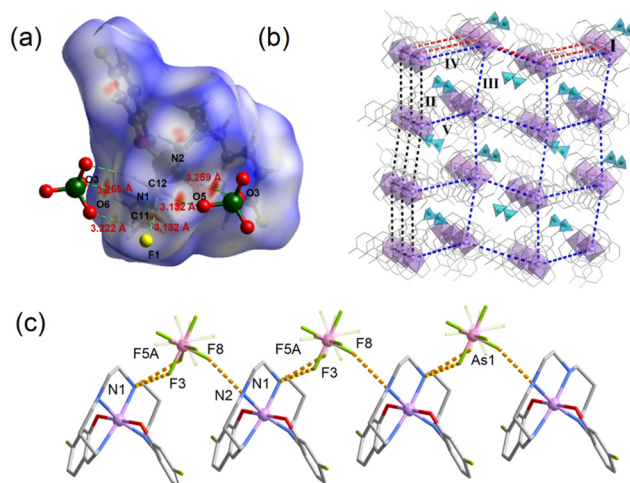


**Fig. 4** (a) Hirshfeld surface analysis of complex **1** at 60 K, showing the $d_{norm}$ surfaces of the mono-cationic unit. (b) Crystal packing of complex **1** at 300 K, viewed along the *a* axis. (c) View of the 1D hydrogen-bond chain of complex **2**.

molecular interactions at both 60 K and 300 K, without forming a one-dimensional chain structure.

The crystal packing of complex **1** at 300 K shows loosely arranged $[Mn(4F\text{-}sal_2323)]^+$ cations with no significant short-contact interactions (Fig. 4b). The nearest Mn···Mn distances are 7.764 Å at 60 K and 7.863 Å at 300 K along the *a* axis, providing sufficient space for coordination geometry changes required for SCO. This results in hysteretic SCO behavior with a 10 K thermal hysteresis loop. Additionally, a substantial decrease in octahedral distortion parameters is observed when cooling from 300 to 60 K, indicating significant structural changes. Temperature-dependent permittivity measurements on complex **1** show a typical in-phase step change of the dielectric parameter in the 70–100 K range, corresponding to the SCO transition temperature (Fig. 5). The variation in dielectric constant was 0.43, consistent with the previously reported $\Delta\varepsilon'$ ($\Delta\varepsilon' = \varepsilon'_{HS} - \varepsilon'_{LS}$), where $\varepsilon'_{HS}$ and $\varepsilon'_{LS}$ represent the dielectric constants for the HS and LS states, respectively. This change is attributed to local structural modifications at the SCO centers, leading to significant conformational adjustments, especially the pronounced swing motion of the fluorobenzene rings.

The fingerprint plots of complexes **2–5** at 300 K show stronger intermolecular interactions compared to complex **1**, with more prominent red spots (Fig. S8†). The hydrogen bond distances (Å) and angles (°) for complexes **2–5** are listed in Tables S15 and S16.† These interactions, particularly N–H···X hydrogen bonds, are crucial for the hysteretic SCO in the $ClO_4^-$ complex and gradual SCO in $AsF_6^-$, $PF_6^-$, $ReO_4^-$, and $NO_3^-$ analogues. For example, in complex **2**, N–H···F interactions have distances of 3.029 Å and 3.066(11) Å at 300 K, decreasing to 2.960(6) Å and 3.024(6) Å at 35 K (Fig. 4c and Table S15†). These interactions form continuous supramolecular chains with parallel cations and zigzag anions, making the chain more rigid. It is noteworthy that the relatively small sizes of $ReO_4^-$ and $NO_3^-$ in complexes **4** and **5** lead to tighter molecular packing. Specifically, complex **4** exhibits the shortest Mn···Mn distance along the *a*-axis (7.5155 Å) in the series, while complex **5** shows the shortest Mn···Mn distance along

the *b*-axis (8.2355 Å) (Fig. S9 and Table S16†). This closer packing stabilizes the LS state and restricts ligand flexibility through strong hydrogen bonding, preventing distortion of $Mn^{III}$ coordination geometry and hindering spin transition of the $[Mn(4F\text{-}sal_2323)]^+$ cation. As a consequence, complexes **4** and **5** exhibit incomplete SCO and maintain LS characteristics. Conversely, the larger size of the $AsF_6^-$ and $PF_6^-$ anions in complexes **2** and **3** cause longer Mn···Mn distances and looser packing, favoring the HS state. However, this also increases C–H···F interactions, leading to incomplete SCO and maintaining HS characteristics. The $AsF_6^-$ system shows a disordered anion suggesting it doesn't quite fit in the hole in the structure. Indeed, subtle variations in the anion can lead to shifts in the SCO transition temperature, changes in the hysteresis width, or fundamental changes in the nature of the transition, such as a transition from abrupt to gradual.

The influences of counterions on the coordination environment are also reflected by the redox potential of the complexes. Therefore, electrochemical investigations for complexes **1–5** were performed using cyclic voltammetry (CV) in acetonitrile solution containing **1–5** (1 mM) with 0.2 M ($^nBu_4N)PF_6$ as the electrolyte.[53] The voltammograms are depicted in Fig. 6a and S11.† The cyclic voltammetry data are given in
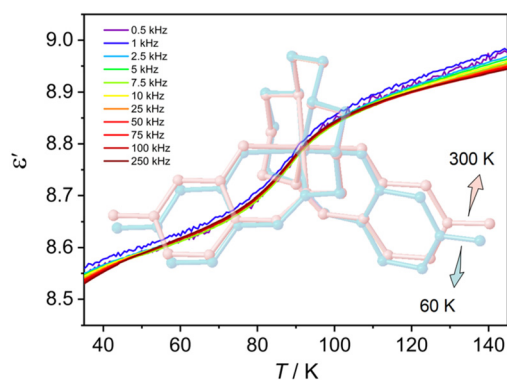


**Fig. 5** Temperature dependence of the in-phase of the dielectric parameter ($\varepsilon'$) for complex **1** in cooling mode. The background image shows the overlapped molecular structures of **1** at 60 K (blue) and 300 K (pale pink).
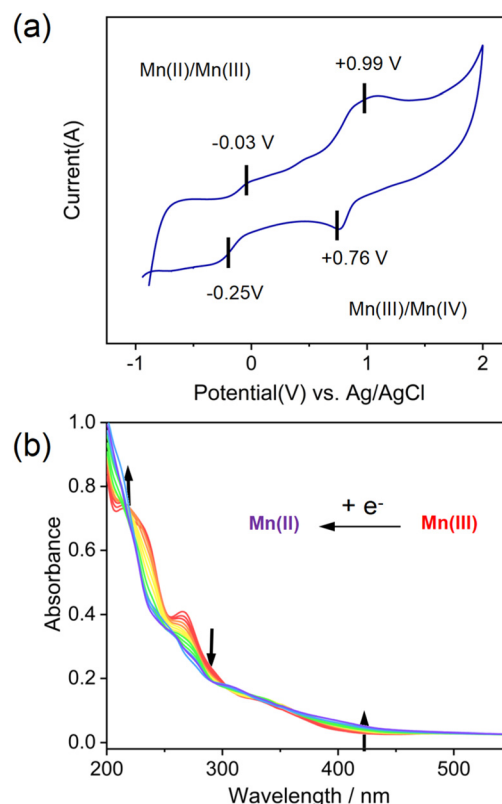


**Fig. 6** (a) Cyclic voltammograms of **1** in 0.2 M ($^nBu_4N)PF_6$/MeCN with a scan rate of 0.1 V s$^{-1}$. (b) Solution-state spectroelectrochemistry of **1** in 0.2 M ($^nBu_4N)PF_6$/MeCN over the potential range of 0.0 V to −0.65 V. Ag/AgCl was selected as the reference. Arrows indicate the change in absorbance with the application of potential.

**Table 2** Cyclic voltammogram data of complexes **1–5** in MeCN containing 0.2 M ($^n$Bu$_4$N)PF$_6$ as the electrolyte with a scan rate of 0.1 V s$^{-1}$

| Complex | Mn(III)/Mn(II) | | | Mn(III)/Mn(IV) | | |
|---|---|---|---|---|---|---|
| | $E_{pc}$/V | $E_{pa}$/V | $E_{1/2}$/V | $E_{pc}$/V | $E_{pa}$/V | $E_{1/2}$/V |
| **1** | −0.25 | −0.03 | −0.14 | 0.99 | 0.76 | 0.88 |
| **2** | −0.18 | −0.01 | −0.10 | 0.79 | 0.75 | 0.77 |
| **3** | −0.19 | −0.06 | −0.13 | 0.79 | 0.73 | 0.76 |
| **4** | −0.19 | −0.09 | −0.14 | 0.78 | 0.74 | 0.76 |
| **5** | −0.28 | −0.01 | −0.15 | 0.83 | 0.74 | 0.79 |

**Table 3** Calculated $\rho$(N$_{amine}$), $\rho$(N$_{imine}$), $\rho$(O), and experimental SCO temperature ($T_{1/2}$) values of complexes **1–5**

| | **1** | **2** | **3** | **4** | **5** |
|---|---|---|---|---|---|
| O1 | −0.65232 | −0.64537 | −0.63659 | −0.64348 | −0.64314 |
| O2 | −0.64484 | −0.65067 | −0.64782 | −0.65165 | −0.63744 |
| N3 | −0.49945 | −0.51961 | −0.52063 | −0.52629 | −0.52835 |
| N4 | −0.45097 | −0.50409 | −0.5004 | −0.50342 | −0.49621 |
| N5 | −0.28012 | −0.2711 | −0.27476 | −0.27468 | −0.27758 |
| N6 | −0.27457 | −0.27306 | −0.28065 | −0.27911 | −0.26736 |
| $T_{1/2}$ | 95 | 82 | 92 | 192 | 294 |

Table 2. The voltammograms of complexes **1–5** exhibited a quasi-reversible oxidation process of the Mn$^{III}$ to Mn$^{IV}$ at approximately 0.76–0.88 V *vs.* Ag/AgCl. Additionally, the reduction from Mn$^{III}$ to Mn$^{II}$ occurred in the range of −0.10 and −0.15 V. The reduction potentials follow the order of **5** ($E_{1/2}$ = −0.15 V) > **4** ($E_{1/2}$ = −0.14 V) ≈ **1** ($E_{1/2}$ = −0.14 V) > **3** ($E_{1/2}$ = −0.13 V) > **2** ($E_{1/2}$ = −0.10 V), while the oxidation potentials increase in the order of **3** ($E_{1/2}$ = 0.76 V) ≈ **4** ($E_{1/2}$ = 0.76 V) < **2** ($E_{1/2}$ = 0.77 V) < **5** ($E_{1/2}$ = 0.79 V) < **1** ($E_{1/2}$ = 0.88 V), indicating a significant influence of the counterions on the redox properties of these complexes.

To gain further insight into the redox behavior, we performed *in situ* spectroelectrochemical measurements on complexes **1–5** in 0.2 M ($^n$Bu$_4$N) PF$_6$/MeCN between 0.0 V and −0.65 V *vs.* Ag/AgCl (Fig. 6b and S12†). During the reduction process of complex **1**, the intensity of the LMCT band originating from phenolate → Mn$^{III}$ (P$_\pi$ → d$_{\sigma^*}$) at 260 nm decreased, accompanied by the appearance of a new band at 410 nm that can be attributed to a CT from phenolate → Mn$^{II}$. Similarly, the absorption spectra of complexes **2–5** exhibited a decrease in intensity at 260 nm and an increase at 400 nm. The presence of the isosbestic points at 295 and 480 nm indicates that a single reduction process occurs, confirming the quasi-reversible nature of the transition between [Mn$^{III}$(4F-sal$_2$-323)]$^+$ and [Mn$^{II}$(4F-sal$_2$-323)], as observed in the cyclic voltammogram.

All the complexes exhibit nearly the same packing patterns, except for differences in the number and distances of intermolecular hydrogen bonds. Magnetic measurements and structural analysis indicate that the sizes of the counterions play an important role in the coordination field strength at the Mn center and the redox potential. These hydrogen bond interactions involve the amino nitrogen coordinated to Mn. It is expected that these interactions will affect the charge density on the nitrogen atom and the coordination strength with Mn, thereby influencing the spin crossover (SCO) transition temperature. To qualitatively explain this, we performed density functional theory (DFT) calculations.[54]

We conducted the theoretical MO calculations on the series of 4F-323 ligands and performed DFT calculations in the Gaussian 16 package. The B3LYP Hamiltonian with the 6-311G-(d,p) basis set was selected.[55] The geometry of complexes was extracted from the crystal diffraction structure data with optimization of hydrogen atoms. Only the ligand portion was subjected to the energy calculation, additional keywords were included to save natural atom orbitals (NAOs), and NAO-based analysis was further conducted using Multiwfn to characterize the atomic charge of atoms involved in coordination.[56,57] Because the crystal field is highly sensitive to the charge distribution or electron population of the coordinating atom, the atomic charge on the amine nitrogen could be utilized to qualitatively evaluate the influence of the counterion on crystal field strength and SCO properties. It should be pointed out that natural population analysis (NPA) provides more accurate results compared to Mulliken population analysis, especially when high-precision basis sets are employed.[58] Therefore, natural orbital population analysis was conducted using the natural bond orbital (NBO) method.

The natural charges of the six coordinating atoms along with the electron density at nitrogen ($\rho$(N/O)) were calculated (Table 3). These values vary depending on the counterion, with $\rho$(N3) and $\rho$(N4) in complex **1** being significantly lower than those in the other complexes. This discrepancy is due to the weaker hydrogen bonding interactions between the amino nitrogen (N3/N4) and the ClO$_4^-$ anion in complex **1**. Furthermore, a negative correlation is observed between $T_{1/2}$ and $\rho$(N3) (Fig. S13†). The molecular electrostatic potential surfaces for complexes **1–5** are depicted in Fig. S8.† Fingerprint plots for complexes **2–5** at 300 K reveal more prominent red spots compared to complex **1** when the complex cation surfaces are mapped using the $d_{norm}$ function. Analysis at 300 K indicates that the H···F and H···O interactions are among the primary intermolecular interactions in complexes **2–5**, contributing 32.1%, 32.1%, 20.2%, and 15.3%, respectively, of all interactions. Notably, these interactions remain relatively unchanged or are slightly increased during the cooling process of complexes **2–5**. The amino nitrogen atoms exhibit more electronegative characteristics in complexes **2–5**, with the amino N atoms in these complexes being more negative than those in complex **1**. The atomic charge on the imine nitrogen atoms, extracted through natural population analysis, further confirms these observations.

## Conclusions

In summary, we described the synthesis and crystal structures of a series of new salts based on the six-coordinated mononuclear manganese(III) Schiff-base complex cation [Mn(4F-

sal$_2$323)]X. Variable-temperature single-crystal X-ray crystallography analysis and magnetic measurements provided firm evidence for the counterion effects of this system. Subtle variations in the anion can lead to shifts in the spin crossover transition temperature, changes in the hysteresis width, or fundamental changes in the nature of the transition, such as a transition from abrupt to gradual. Careful evaluation of the supramolecular structures of these complexes revealed strong correlations between supramolecular packing forces and their SCO behavior. The electron population analysis at the ligating nitrogen atom in a metal-free ligand by means of the DFT MO method provides one of the most convenient and powerful ways to explain and predict the SCO temperature. Our work provides relevant references for controlling spin transition behavior through modulation of intermolecular interactions and for the development of solid-state spin transition devices.

## Conflicts of interest

There are no conflicts to declare.

## Data availability

The data supporting this article have been included as part of the ESI† and can be obtained freely by asking the authors.

## Acknowledgements

## References

1 D. C. Ashley and E. Jakubikova, *Coord. Chem. Rev.*, 2017, **337**, 97–111.

2 M. A. Halcrow, *Chem. Soc. Rev.*, 2011, **40**, 4119–4142.

3 J. Tao, R. J. Wei, R. B. Huang and L. S. Zheng, *Chem. Soc. Rev.*, 2012, **41**, 703–737.

4 B. Weber, *Coord. Chem. Rev.*, 2009, **253**, 2432–2449.

5 V. B. Jakobsen, S. Chikara, J.-X. Yu, E. Dobbelaar, C. T. Kelly, X. Ding, F. Weickert, E. Trzop, E. Collet, H.-P. Cheng, G. G. Morgan and V. S. Zapf, *Inorg. Chem.*, 2020, **60**, 6167–6175.

6 V. B. Jakobsen, E. Trzop, L. C. Gavin, E. Dobbelaar, S. Chikara, X. Ding, K. Esien, H. Muller-Bunz, S. Felton, V. S. Zapf, E. Collet, M. A. Carpenter and G. G. Morgan, *Angew. Chem., Int. Ed.*, 2020, **59**, 13305–13312.

7 R. Ohtani and S. Hayami, *Chem. – Eur. J.*, 2017, **23**, 2236–2248.

8 I. C. Y. Hou, L. Li, H. Zhang and P. Naumov, *Smart Mol.*, 2024, **2**, e20230031.

9 W. Zhang and K. J. Gaffney, *Acc. Chem. Res.*, 2015, **48**, 1140–1148.

10 M.-J. Shang, H.-H. Lu, Q. Liu, R.-H. Zhou, H.-Y. Sun, Z. Shao, L. Zhao, Y.-S. Meng and T. Liu, *Inorg. Chem. Front.*, 2024, **11**, 8704–8714.

11 X. Xiao, Z. J. Chen, R. J. Varley and C. H. Li, *Smart Mol.*, 2024, **2**, e20230028.

12 M. A. Halcrow, *Coord. Chem. Rev.*, 2009, **253**, 2493–2514.

13 C. Zhang, X. Jiang, C. Wang, Z. Liu, B. Xu and W. Tian, *Smart Mol.*, 2025, **1**, e20240054.

14 A. Bousseksou, G. Molnar, L. Salmon and W. Nicolazzi, *Chem. Soc. Rev.*, 2011, **40**, 3313–3335.

15 K. Senthil Kumar and M. Ruben, *Coord. Chem. Rev.*, 2017, **346**, 176–205.

16 S. Brooker, *Chem. Soc. Rev.*, 2015, **44**, 2880–2892.

17 M. M. Khusniyarov, *Chem. – Eur. J.*, 2016, **22**, 15178–15191.

18 G. Aromí, L. A. Barrios, O. Roubeau and P. Gamez, *Coord. Chem. Rev.*, 2011, **255**, 485–546.

19 Z.-P. Ni, J.-L. Liu, M. N. Hoque, W. Liu, J.-Y. Li, Y.-C. Chen and M.-L. Tong, *Coord. Chem. Rev.*, 2017, **335**, 28–43.

20 D. J. Harding, P. Harding and W. Phonsri, *Coord. Chem. Rev.*, 2016, **313**, 38–61.

21 S. Hayami, Y. Komatsu, T. Shimizu, H. Kamihata and Y. H. Lee, *Coord. Chem. Rev.*, 2011, **255**, 1981–1990.

22 M. S. Shongwe, K. S. Al-Barhi, M. Mikuriya, H. Adams, M. J. Morris, E. Bill and K. C. Molloy, *Chem. – Eur. J.*, 2014, **20**, 9693–9701.

23 P. G. Sim and E. Sinn, *J. Am. Chem. Soc.*, 1981, **103**, 241–243.

24 P. N. Martinho, B. Gildea, M. M. Harris, T. Lemma, A. D. Naik, H. Muller-Bunz, T. E. Keyes, Y. Garcia and G. G. Morgan, *Angew. Chem., Int. Ed.*, 2012, **51**, 12597–12601.

25 A. V. Kazakova, A. V. Tiunova, D. V. Korchagin, G. V. Shilov, E. B. Yagubskii, V. N. Zverev, S. C. Yang, J. Y. Lin, J. F. Lee, O. V. Maximova and A. N. Vasiliev, *Chem. – Eur. J.*, 2019, **25**, 10204–10213.

26 R. W. Hogue, S. Singh and S. Brooker, *Chem. Soc. Rev.*, 2018, **47**, 7303–7338.

27 I. A. Kühne, A. Barker, F. Zhang, P. Stamenov, O. O'Doherty, H. Müller-Bunz, M. Stein, B. J. Rodriguez and G. G. Morgan, *J. Phys.: Condens. Matter*, 2020, **32**, 404002.

28 E. Dobbelaar, V. B. Jakobsen, E. Trzop, M. Lee, S. Chikara, X. Ding, H. Muller-Bunz, K. Esien, S. Felton, M. A. Carpenter, E. Collet, G. G. Morgan and V. S. Zapf, *Angew. Chem., Int. Ed.*, 2022, **61**, e202114021.

29 S. Ghosh, S. Bagchi, M. Das, S. Kamilya and A. Mondal, *Dalton Trans.*, 2020, **49**, 14776–14780.

30 S. Ghosh, S. Bagchi, S. Kamilya and A. Mondal, *Dalton Trans.*, 2021, **50**, 4634–4642.

31 G. G. Morgan, K. D. Murnaghan, H. Muller-Bunz, V. McKee and C. J. Harding, *Angew. Chem., Int. Ed.*, 2006, **45**, 7192–7195.

32 A. Barker, C. T. Kelly, I. A. Kuhne, S. Hill, J. Krzystek, P. Wix, K. Esien, S. Felton, H. Muller-Bunz and G. G. Morgan, *Dalton Trans.*, 2019, **48**, 15560–15566.

33 A. J. Fitzpatrick, S. Stepanovic, H. Müller-Bunz, M. A. Gruden-Pavlović, P. García-Fernández and G. G. Morgan, *Dalton Trans.*, 2016, **45**, 6702–6708.

34 M. M. Harris, I. A. Kühne, C. T. Kelly, V. B. Jakobsen, R. Jordan, L. O'Brien, H. Müller-Bunz, S. Felton and G. G. Morgan, *Cryst. Growth Des.*, 2023, **23**, 3996–4012.

35 V. B. Jakobsen, E. Trzop, E. Dobbelaar, L. C. Gavin, S. Chikara, X. Ding, M. Lee, K. Esien, H. Muller-Bunz, S. Felton, E. Collet, M. A. Carpenter, V. S. Zapf and G. G. Morgan, *J. Am. Chem. Soc.*, 2022, **144**, 195–211.

36 A. V. Tiunova, A. V. Kazakova, D. V. Korchagin, G. V. Shilov, L. V. Zorina, S. V. Simonov, K. V. Zakharov, A. N. Vasiliev and E. B. Yagubskii, *Chem. – Eur. J.*, 2021, **27**, 17609–17619.

37 A. V. Tiunova, A. V. Kazakova, D. V. Korchagin, G. V. Shilov, K. V. Zakharov, A. N. Vasiliev and E. B. Yagubskii, *New J. Chem.*, 2022, **46**, 16880–16888.

38 I. A. Kühne, L. C. Gavin, M. Harris, B. Gildea, H. Müller-Bunz, M. Stein and G. G. Morgan, *J. Appl. Phys.*, 2021, **129**, 213903.

39 I. A. Kühne, A. Ozarowski, A. Sultan, K. Esien, A. B. Carter, P. Wix, A. Casey, M. Heerah-Booluck, T. D. Keene, H. Müller-Bunz, S. Felton, S. Hill and G. G. Morgan, *Inorg. Chem.*, 2022, **61**, 3458–3471.

40 H.-W. Zhou, S.-Z. Zhao, C.-Y. Qin, H.-Z. Zhang, Y.-H. Li and S. Wang, *J. Mol. Struct.*, 2023, **1287**, 135706.

41 S. Wang, W.-T. Xu, W.-R. He, S. Takaishi, Y.-H. Li, M. Yamashita and W. Huang, *Dalton Trans.*, 2016, **45**, 5676–5688.

42 A. J. Fitzpatrick, E. Trzop, H. Müller-Bunz, M. M. Dîrtu, Y. Garcia, E. Collet and G. G. Morgan, *Chem. Commun.*, 2015, **51**, 17540–17543.

43 C.-Y. Qin, S.-Z. Zhao, H.-Y. Wu, Y.-H. Li, Z.-K. Wang, Z. Wang and S. Wang, *Dalton Trans.*, 2021, **50**, 5899–5910.

44 M. Shatruk, H. Phan, B. A. Chrisostomo and A. Suleimenova, *Coord. Chem. Rev.*, 2015, **289-290**, 62–73.

45 S. Wang, Y.-J. Li, F.-F. Ju, W.-T. Xu, K. Kagesawa, Y.-H. Li, M. Yamashita and W. Huang, *Dalton Trans.*, 2017, **46**, 11063–11077.

46 C. T. Kelly, V. B. Jakobsen, R. Jordan, S. Felton, H. Müller–Bunz and G. G. Morgan, *Chem. – Eur. J.*, 2025, **31**, 9.

47 S. Wang, Y. H. Li and W. Huang, *Eur. J. Inorg. Chem.*, 2015, **2015**, 2237–2244.

48 S. Sundaresan, I. A. Kühne, C. Evesson, M. M. Harris, A. J. Fitzpatrick, A. Ahmed, H. Müller-Bunz and G. G. Morgan, *Polyhedron*, 2021, **208**, 115386.

49 Y. Chen, F. Cao, R.-M. Wei, Y. Zhang, Y.-Q. Zhang and Y. Song, *Dalton Trans.*, 2014, **43**, 3783–3791.

50 H.-Z. Zhang, H.-W. Zhou, P.-Y. Xu, C.-Y. Qin, S.-Z. Zhao, Y.-H. Li and S. Wang, *Polyhedron*, 2024, **248**, 116757.

51 B. Gildea, M. M. Harris, L. C. Gavin, C. A. Murray, Y. Ortin, H. Muller-Bunz, C. J. Harding, Y. Lan, A. K. Powell and G. G. Morgan, *Inorg. Chem.*, 2014, **53**, 6022–6033.

52 S. Bagchi, S. Kamilya, S. Mehta, S. Mandal, A. Bandyopadhyay, A. Narayan, S. Ghosh and A. Mondal, *Dalton Trans.*, 2023, **52**, 11335–11348.

53 S. Ghosh, S. Bagchi, S. Kamilya, S. Mehta, D. Sarkar, R. Herchel and A. Mondal, *Dalton Trans.*, 2022, **51**, 7681–7694.

54 S. Amabilino and R. J. Deeth, *Inorg. Chem.*, 2017, **56**, 2602–2613.

55 R. Krishnan, J. S. Binkley, R. Seeger and J. A. Pople, *J. Chem. Phys.*, 1980, **72**, 650–654.

56 T. Lu, *J. Chem. Phys.*, 2024, **161**, 082503.

57 T. Lu and F. Chen, *J. Comput. Chem.*, 2011, **33**, 580–592.

58 A. Kimura and T. Ishida, *ACS Omega*, 2018, **3**, 6737–6747.